

ARTICLE

Open Access

# Microwave synthesis of gram scale millimeter size layered transition metal oxide crystals

Rami Elkaffas<sup>1</sup>, Ayman Rezk<sup>2</sup>, Shanavas Shajahan<sup>1</sup>, Israr Ahmed<sup>1</sup>, Dalaver H. Anjum<sup>3</sup>, Haider Butt<sup>4</sup>, Ammar Nayfeh<sup>2</sup> and Yarjan Abdul Samad<sup>1,5</sup>

## Abstract

Layered transition metal oxides (TMOs) have been utilized for centuries for their abundance and diverse applications in various fields. Developing efficient synthesis methods of layered TMOs is crucial for exploring novel properties and potential applications. This work introduces a direct microwave synthesis method for producing transition metal oxides and crystals. Using alpha molybdenum trioxide as a representative example, a microwave synthesis protocol is outlined for the rapid and scalable synthesis of layered transition metal oxides. Transition metal oxides have been synthesized using various state-of-the-art (SOTA) techniques, such as hydrothermal and sol-gel, among others. In contrast to these established methods, our direct microwave process is simple, requiring only a microwave and minimal handling, and it is highly scalable (1 g/h of  $\alpha$ -MoO<sub>3</sub> crystals). Additionally, it consumes just 0.5 kWh of energy per gram of  $\alpha$ -MoO<sub>3</sub>, which is 8-140 times better than typical SOTA methods. It is environmentally friendly as it produces ~10-150 times less CO<sub>2</sub> emissions (0.3 kg CO<sub>2</sub> eq) compared to SOTA methods. It produces long crystals with a length of up to 8 mm, which is comparable to hazardous chemical and physical vapor deposition methods. We further demonstrate the advantages of these high-quality crystals by fabricating a MoO<sub>3</sub>-based Metal-Interlayer-Oxide-Semiconductor (MIOS) memristor incorporating an ultrathin Al<sub>2</sub>O<sub>3</sub> interlayer. The device exhibits low SET (~ -2 V) and RESET (~2 V) voltages with stable endurance over multiple cycles, attributed to field-driven oxygen vacancy migration. These findings establish microwave synthesis as a transformative approach for producing high-performance metal oxides and underscore the significant potential of MoO<sub>3</sub> for next-generation energy-efficient and reliable memory technologies.

## Introduction

Layered Transition metal oxides have garnered significant attention from researchers due to their remarkable electrical<sup>1</sup>, optical<sup>2</sup>, and mechanical properties<sup>3</sup>. Among these transition metal oxides (TMOs), molybdenum trioxide (MoO<sub>3</sub>) is the most studied, owing to its ability to adopt diverse morphologies such as nanorods<sup>4</sup>, nanotubes<sup>5</sup>, nanobelts<sup>6</sup>, nanoplatelets<sup>7</sup>, nanofibers<sup>8</sup>, nanoflowers<sup>9</sup>, nanospheres<sup>10</sup>, and nanoflakes<sup>11</sup>. These diverse morphologies arise from MoO<sub>3</sub>'s inherent layered structure and

intriguing physical properties<sup>12</sup>. Functioning as an n-type semiconductor with a wide bandgap ranging from 2.8 to 3.6 eV<sup>13</sup>, MoO<sub>3</sub> exhibits versatile applications, including photochromic<sup>14</sup> and electrochromic devices<sup>15</sup>, photoconductive devices<sup>16</sup>, smart windows<sup>17</sup>, thermoelectric materials<sup>18</sup>, catalysis<sup>19</sup>, lithium-ion batteries<sup>20</sup>, supercapacitors<sup>21</sup>, solar cells<sup>22</sup>, and gas sensors<sup>23</sup>.

MoO<sub>3</sub> exists in three distinct crystalline polymorphs ( $\alpha$ ,  $\beta$ , h-MoO<sub>3</sub>), each exhibiting unique structural characteristics and properties<sup>12</sup>. The first polymorph,  $\alpha$ -MoO<sub>3</sub>, presents a dynamically stable phase featuring double layers of [MoO<sub>6</sub>] octahedral units<sup>24</sup>. These layers are arranged parallel to the (010) plane, offering open channels conducive to ion intercalation, thus enabling efficient charge storage<sup>25</sup>. In contrast, the  $\beta$ -MoO<sub>3</sub> polymorph adopts a three-dimensional structure formed by corner-sharing

Correspondence: Yarjan Abdul Samad (Yarjan.abdulsamad@ku.ac.ae)

<sup>1</sup>Department of Aerospace Engineering, Khalifa University of Science and Technology, Abu Dhabi, United Arab Emirates

<sup>2</sup>Department of Electrical Engineering, Khalifa University of Science and Technology, Abu Dhabi, United Arab Emirates

Full list of author information is available at the end of the article

© The Author(s) 2026



**Open Access** This article is licensed under a Creative Commons Attribution 4.0 International License, which permits use, sharing, adaptation, distribution and reproduction in any medium or format, as long as you give appropriate credit to the original author(s) and the source, provide a link to the Creative Commons licence, and indicate if changes were made. The images or other third party material in this article are included in the article's Creative Commons licence, unless indicated otherwise in a credit line to the material. If material is not included in the article's Creative Commons licence and your intended use is not permitted by statutory regulation or exceeds the permitted use, you will need to obtain permission directly from the copyright holder. To view a copy of this licence, visit <http://creativecommons.org/licenses/by/4.0/>.

[MoO<sub>6</sub>] octahedral units<sup>26</sup>, indicative of a metastable monoclinic phase<sup>27</sup>. Meanwhile, the h-MoO<sub>3</sub> polymorph, also metastable, showcases a hexagonal crystalline structure characterized by zigzag chains of [MoO<sub>6</sub>] octahedra<sup>28</sup>, facilitating one-dimensional tunnel behavior<sup>29</sup>. Among the crystal structures of MoO<sub>3</sub>, α-MoO<sub>3</sub> is particularly widely studied, the most studied phase due to its unique layered architecture<sup>30</sup>. A key characteristic of α-MoO<sub>3</sub> is its layered structure, which can accommodate large quantities of positive ions in its tetrahedral and octahedral holes and extension channels<sup>31</sup>, enabling bandgap manipulation<sup>32</sup>. This layered configuration enhances charge transfer capabilities<sup>33</sup>, improving its electrochemical properties<sup>34</sup>. Various synthesis methods have been employed to prepare α-MoO<sub>3</sub>, each with advantages and limitations. State-of-the-art (SOTA) techniques, including this work, are compared in detail.

To the best of our knowledge, this is the first work to synthesize α-MoO<sub>3</sub> from molybdenum disulfide (MoS<sub>2</sub>; a naturally occurring ore of Mo metal) as a starting material for large-scale production. Our in-depth analysis of SOTA methods demonstrates that microwave synthesis offers a compelling alternative for α-MoO<sub>3</sub> production due to a combination of cost-effectiveness, speed, simplicity, scalability, crystal length, and energy efficiency. The crystal length achieved through microwave synthesis is approximately 7 mm, surpassing most common methods except for Chemical Vapor Deposition (CVD) and Physical Vapor Deposition (PVD), which produce crystals in a similar to higher size range. Microwave synthesis boasts a rapid production time of approximately 2 min to start forming MoO<sub>3</sub> crystals, which is ~50–600 times faster than SOTA methods. The process is simple and scalable, requiring only a microwave, minimal handling, and only 1 h to produce 1 gram of α-MoO<sub>3</sub>, up to 600 times better than SOTA. Additionally, microwave synthesis is the most energy-efficient method, consuming just 0.5 kWh per gram of α-MoO<sub>3</sub>, up to 140 times better than SOTA methods. These features make microwave synthesis more practical and efficient for α-MoO<sub>3</sub> production. In contrast to conventional methods in literature, this work pioneers the direct synthesis of MoO<sub>3</sub> from naturally abundant MoS<sub>2</sub> as the starting material, eliminating costly and energy-intensive intermediate purification steps and offering a cost-effective and scalable route for the large scale of MoO<sub>3</sub> and TMOs production.

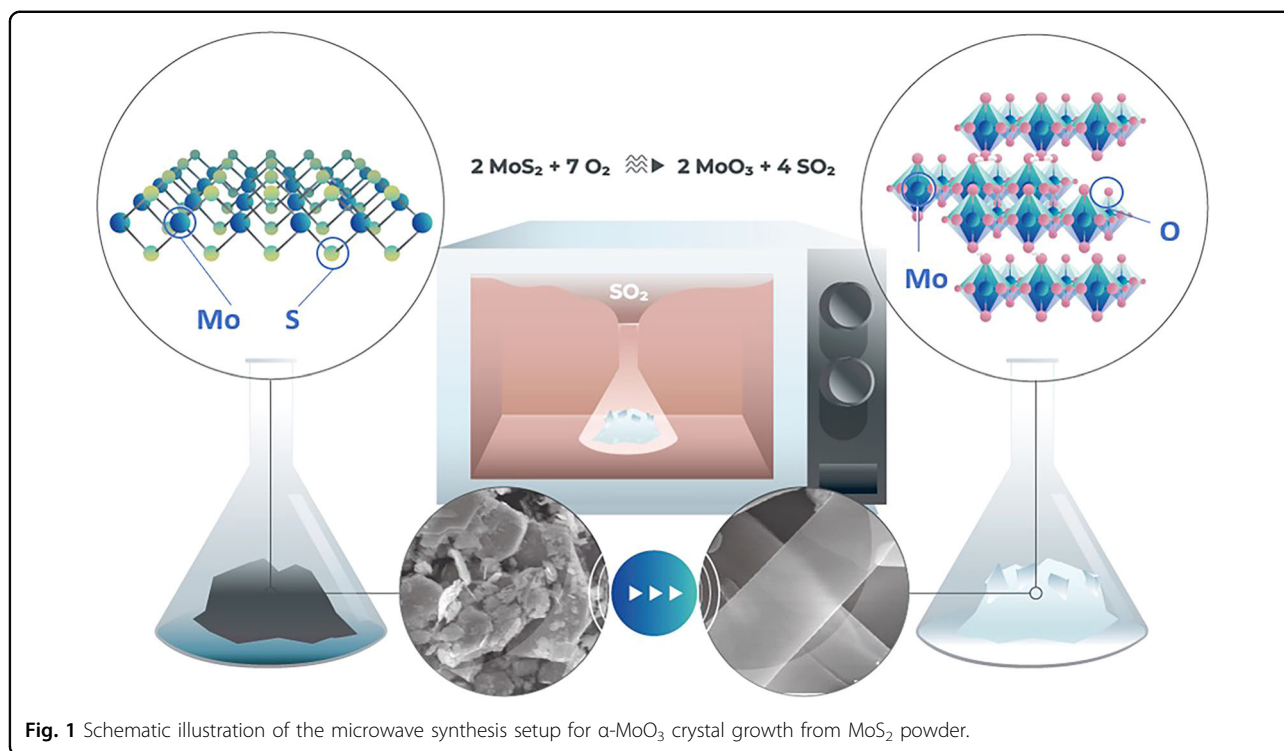
### Mechanism growth of alpha molybdenum trioxide crystals

Various mechanisms (i.e., dielectric loss, Joule loss, and magnetic loss) are briefly discussed to understand the dominant heating mechanism during microwave irradiation comprehensively; however, the different interactions between materials and microwaves cannot be explained by a single theory. In general, microwave power absorption

and penetration depth must be considered for the microwave processing of materials. The former,  $P$  (W/m<sup>3</sup>), is evaluated by Eq. (S1). The latter,  $D_p$  (m), represents a depth inside the material where the power of the wave reaches. Calculated according to Eq. (S2): Regarding Eqs. (S1) and (S2), materials' electrical conductivity, permittivity, and permeability play vital roles during microwave heating. Three different mechanisms that would contribute to microwave heating are presented in Eq. (S1): Conduction (Joule) loss (first term, W/m<sup>3</sup>) is a dominant heating mechanism of materials with high electrical conductivity, such as metals. This mechanism results from eddy current loss generated in an alternating magnetic field and mainly depends on the material's electrical conductivity. Dielectric loss (second term, W/m<sup>3</sup>) is due to either the polarization of materials and collision of dipoles or the electric charge's collision under an alternating electric field. The dielectric polarization loss includes the polarization of either electron, dipolar, atoms, ions, or interfacial polarization. The contribution of magnetic loss (third term, W/m<sup>3</sup>) to the heating is caused by hysteresis, eddy currents, domain wall, and electron spin resonance in an alternating magnetic field.

Eq. (S2) explains the key difference between conventional and microwave heating methods. The shallow penetration depth of infrared waves during conventional heating results in the heating of the surface of materials followed by heat transfer from the surface toward the core of the sample, whereas a great penetration depth of microwaves during microwave heating results in the volumetric heating of the materials. In microwave heating, the core temperature is higher than the surface due to the heat loss from the surface, which results in the heat transfer from the core toward the sample's surface.

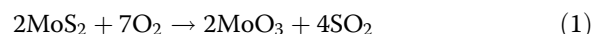
Therefore, factors such as particle size ( $d$ ), shape, and relative density, which directly/indirectly influence these equations, must be considered during microwave heating. For instance, electrical conductivity depends on a pressed sample's particle size, shape, and compaction. Moreover, at a low particle size ratio to penetration depth ( $d/D_p$ ), the particle is considered a transparent material and cannot absorb microwaves. By contrast, at a very high  $d/D_p$  ratio, a major portion of the microwaves are reflected and cannot heat the sample well, and heating is only limited to the sample's surface. In the case of the thermal oxidation of MoS<sub>2</sub> to MoO<sub>3</sub> crystals, Rahman et al.<sup>35</sup> investigated the impact of high-temperature oxidation on the mechanical performance of MoS<sub>2</sub> using ReaxFF, proposing a detailed thermal oxidation mechanism. Initially, oxygen molecules (O<sub>2</sub>) adsorb onto sulfur atoms on the basal plane of MoS<sub>2</sub>, a process that is thermodynamically stable but kinetically hindered under ambient conditions. O<sub>2</sub> dissociates into atomic oxygen upon adsorption, forming covalent



sulfur-oxygen (S-O) bonds. This oxidation leads to volatile sulfur oxides (e.g., SO<sub>2</sub>) that desorb from the surface, creating sulfur vacancies. These vacancies are subsequently filled by oxygen atoms, forming more stable molybdenum-oxygen (Mo-O) bonds. As the oxidation progresses, a molybdenum oxy-sulfide (MoS<sub>2-x</sub>O<sub>x</sub>) solid solution forms, which can further oxidize into MoO<sub>3</sub> at higher temperatures. The process intensifies above 1500 K, with severe crystalline distortion of MoS<sub>2</sub> and significant MoO<sub>3</sub> formation occurring around 1800 K. In 2023, Reidy et al.<sup>36</sup> explained the atomic-scale mechanism of MoS<sub>2</sub> oxidation to MoO<sub>3</sub>. The thermal oxidation of MoS<sub>2</sub> begins with the oxidation of the MoS<sub>2</sub> surface. This process occurs readily at elevated temperatures (e.g., 500 °C in air) and produces MoO<sub>3</sub>. Following the initial oxidation, the volatile species MoO<sub>x</sub> (x can vary) forms and sublimates from the surface. This sublimated species then undergoes vapor-phase mass transport. Then, the MoO<sub>x</sub> species redeposits and crystallizes into  $\alpha$ -MoO<sub>3</sub> on the MoS<sub>2</sub> substrate or nearby surfaces. This results in the growth of crystalline  $\alpha$ -MoO<sub>3</sub>, which is often textured and aligned with the underlying MoS<sub>2</sub> substrate.

This oxidation is exothermic, releasing heat as the reaction progresses. The formation of MoO<sub>3</sub> typically occurs as a gradual transformation of MoS<sub>2</sub>, resulting in MoO<sub>3</sub> as a white crystalline material, as shown in Fig. 1. The reaction progresses by the oxidation of MoS<sub>2</sub>, where sulfur atoms are oxidized to form sulfur dioxide (SO<sub>2</sub>).

Simultaneously, molybdenum atoms combine with oxygen atoms to form MoO<sub>3</sub> according to Eq. 1:



After completion of the oxidation reaction, the MoO<sub>3</sub> crystals are allowed to cool down gradually to ambient temperature before they are collected. Digital images of the process are shown in Supplementary Figs 1 and 2, and  $\alpha$ -MoO<sub>3</sub> crystals are shown in Supplementary Figs. 5 and 6. This process could be used for more members of the TMO family, as shown in Supplementary Figs. 10,11, and 11.

#### Characterization of alpha molybdenum trioxide crystals

The crystal structure of the samples was analyzed using X-ray diffraction (XRD). As shown in Fig. 2a, the distinctive characteristic diffraction peaks at 14.76°, 33.08°, 40.00°, and 50.19°, corresponding to (002), (100), (103), and (105) crystal planes of hexagonal phase MoS<sub>2</sub> are consistent well with standard card of MoS<sub>2</sub> (JCPDS card No. 77-1716)<sup>37</sup>, respectively. Figure 2b reveals peaks at 13.22°, 26.09°, and 39.36°, which correspond to (020), (040), and (060), respectively, of  $\alpha$ -MoO<sub>3</sub>, which possesses an orthorhombic crystal system (JCPDS card No. 05-0508)<sup>38</sup>. The XRD peaks were analyzed employing a modified Scherrer equation to calculate the nano crystallite size, as detailed in Table S2. The (020), (040), and

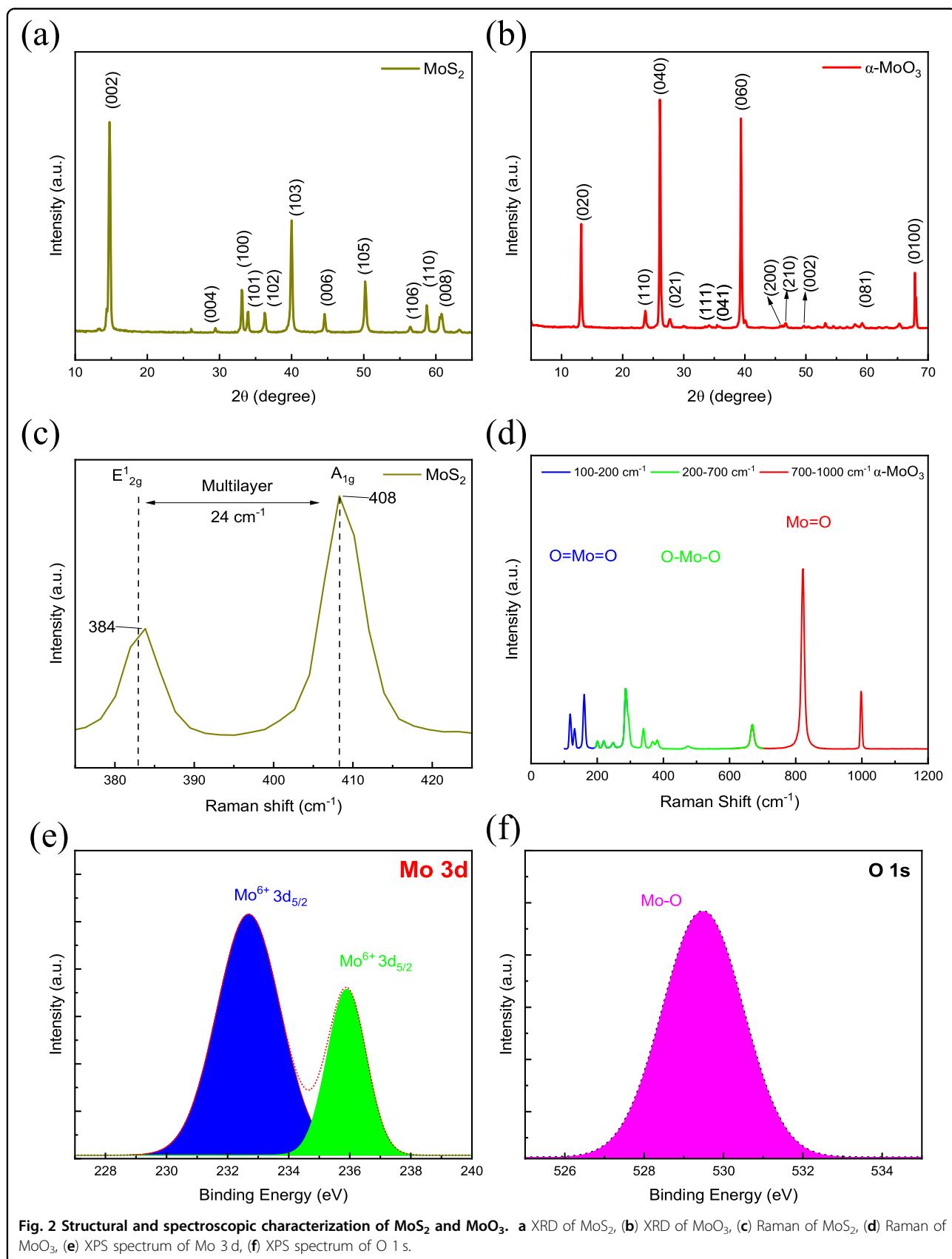


**Fig. 2** Structural and spectroscopic characterization of  $\text{MoS}_2$  and  $\text{MoO}_3$ . **(a)** XRD of  $\text{MoS}_2$ , **(b)** XRD of  $\text{MoO}_3$ , **(c)** Raman of  $\text{MoS}_2$ , **(d)** Raman of  $\text{MoO}_3$ , **(e)** XPS spectrum of Mo 3d, **(f)** XPS spectrum of O 1s.

(060) phases exhibit respective particle sizes ( $D_p$ ) of 38.02, 41.22, and 40.38, along with approximate d-spacing values of 6.7, 3.4, and 2.3, respectively. Notably, the strong specific (020), (040), and (060) peaks confirm the layered crystal structure of  $\alpha$ - $\text{MoO}_3$  and are consistent with highly anisotropic growth along the c-axis<sup>39</sup>. Furthermore, the absence of peaks from other phases, such as  $\text{MoS}_2$ , suggests the high purity of the sample. Raman spectrum (Fig. 2c) of  $\text{MoS}_2$  powder shows characteristic peaks at 384 and 408  $\text{cm}^{-1}$ , corresponding to  $E_{2g}^1$  (in-plane optical vibration of the Mo–S bond in opposite directions)<sup>40</sup> and  $A_{1g}$  (out-of-plane optical vibration of S atoms)<sup>41</sup> active modes, respectively. The 24  $\text{cm}^{-1}$  separation between these two peaks indicates the presence of multilayer  $\text{MoS}_2$ <sup>42</sup>, as the  $\text{MoS}_2$  used was purchased commercially and remained unaltered. Raman spectroscopy for the synthesized confirms the  $\alpha$ - $\text{MoO}_3$  phase (Fig. 2d), with peaks at 997  $\text{cm}^{-1}$  and 822  $\text{cm}^{-1}$  corresponding to asymmetrical and symmetrical stretching vibrations of terminal Mo=O bonds<sup>43</sup>. In contrast, the peak at 669  $\text{cm}^{-1}$  corresponds to asymmetrical stretching vibrations of O–Mo–O bonds along with peaks from 200 to 450  $\text{cm}^{-1}$ <sup>44,45</sup>. Additionally, the peaks between 50 and 200  $\text{cm}^{-1}$  represent the skeletal modes of the chains of  $\text{MoO}_4$  tetrahedra, as reported previously<sup>46,47</sup>. A Raman repeatability study was conducted to test the validity of the material over a number of batches (Supporting Fig. 16).

The XPS detailed spectral analysis (Fig. 2e, f, and Supplementary Fig. 9d) confirms the presence and oxidation states of molybdenum (Mo) and the chemical environment of oxygen (O) in the sample. High-resolution Mo 3d spectrum (Fig. 2e), which can be deconvoluted into two 3d doublets using Gaussian fitting, reveals major peaks at 232.8 eV and 236.0 eV characteristic of  $\text{Mo}^{6+}$  oxidation state,  $3d_{5/2}$  and  $3d_{3/2}$ , respectively, without minor peaks. The O 1s spectrum (Fig. 2f), with a peak around 530.1 eV, corresponds to oxygen in the  $\text{MoO}_3$  lattice.

The SEM images of  $\text{MoS}_2$  in Fig. 3a exhibit an uneven structure with agglomerated particles, revealing defined, multi-layered particles with a flake-like structure and particle size of a few micrometers. Additionally, EDX analysis confirms the purity of the  $\text{MoS}_2$  samples, showing the presence of only molybdenum and sulfur without any other elemental impurities (Supplementary Fig. 8a). The closer magnifications in Fig. 3b, c shows the layered belt-shaped structure of  $\alpha$ - $\text{MoO}_3$ , confirming the successful transformation of  $\text{MoS}_2$  to the pure structure of  $\alpha$ - $\text{MoO}_3$  and their structural uniformity. EDX analysis of the  $\text{MoO}_3$  samples (Supplementary Fig. 8c) also confirms their purity, with only molybdenum and oxygen detected, verifying the absence of other elemental contaminants. In Fig. 3d, e, Optical microscope images of the  $\text{MoO}_3$  show

well-defined, elongated belt-like crystals with lengths between 3 to 7 mm. Crystals were long and stable enough to be handled and gathered to form KU letters (Supplementary Fig. 6). Notably, the crystal lengths observed are among the highest recorded in the literature, up to 7 mm, surpassing all the synthesis methods, with CVD and PVD recording higher lengths in millimeters<sup>48</sup>. Figure 3f–h shows an optical microscope image of the  $\text{MoO}_3$  crystals at different magnifications. Atomic Force Microscopy (AFM) and Conductive Atomic Force Microscopy (C-AFM) were employed to evaluate the structural and electrical properties of the synthesized crystals. Figure 3i presents the topographical AFM image of a representative crystal, revealing a thickness of approximately 5 nm (additional topographical images are provided in Supplementary Fig. 3). The corresponding C-AFM measurement, depicted in Fig. 3j, indicates a current of approximately 30 nA along the crystal. To further explore the correlation between crystal thickness and electrical conductivity, we examined crystals of varying thicknesses. As shown in Supplementary Fig. 4, crystals with thicknesses of 70 nm, 213 nm, and 330 nm exhibited measured currents of 15 nA, 8 nA, and 10 nA, respectively. These observations suggest a potential dependence of charge transport properties on the crystal thickness. Transmission electron microscopy (TEM) images in BF-TEM mode provided compelling evidence for the thin rectangular morphology of the synthesized  $\alpha$ - $\text{MoO}_3$  nanostructures (Fig. 4a). The acquired SAED patterns allowed the measurement of the d-spacings of the crystals, which matched the crystal structure of samples determined with XRD experiments (Supplementary Fig. 7 and Supplementary Table 1). These nanorods' corresponding high-resolution TEM (HRTEM) analysis allowed the visualization of the structure of samples in real space and recorded distance of the well-defined lattice fringes, a hallmark of highly crystalline materials, matched nicely with d-spacing measured by performing the SAED experiments (Fig. 4b). Interestingly, the SAED analysis also unveils a preferential growth direction for the  $\alpha$ - $\text{MoO}_3$  nanobelts on the [001] axis (Fig. 4c, d). This anisotropic crystal structure of  $\alpha$ - $\text{MoO}_3$  is likely responsible for this favored orientation. In this structure, distorted  $[\text{MoO}_6]$  octahedra share corners to form sheets, and pairs of these sheets connect via edges along the [001] direction. These bilayers then weakly stack upon each other via van der Waals forces along the [010] axis. Elemental composition analysis of the samples in TEM-EDS mode revealed high-purity crystals with a composition close to the stoichiometric numbers (see Supplementary Fig. 8f). Furthermore, the STEM-EDS hyperspectrum imaging showed a uniform distribution of Mo and O elements through the regions of the particles (Fig. 4e), which implies a uniform crystal and, hence, the uniform corresponding emergent

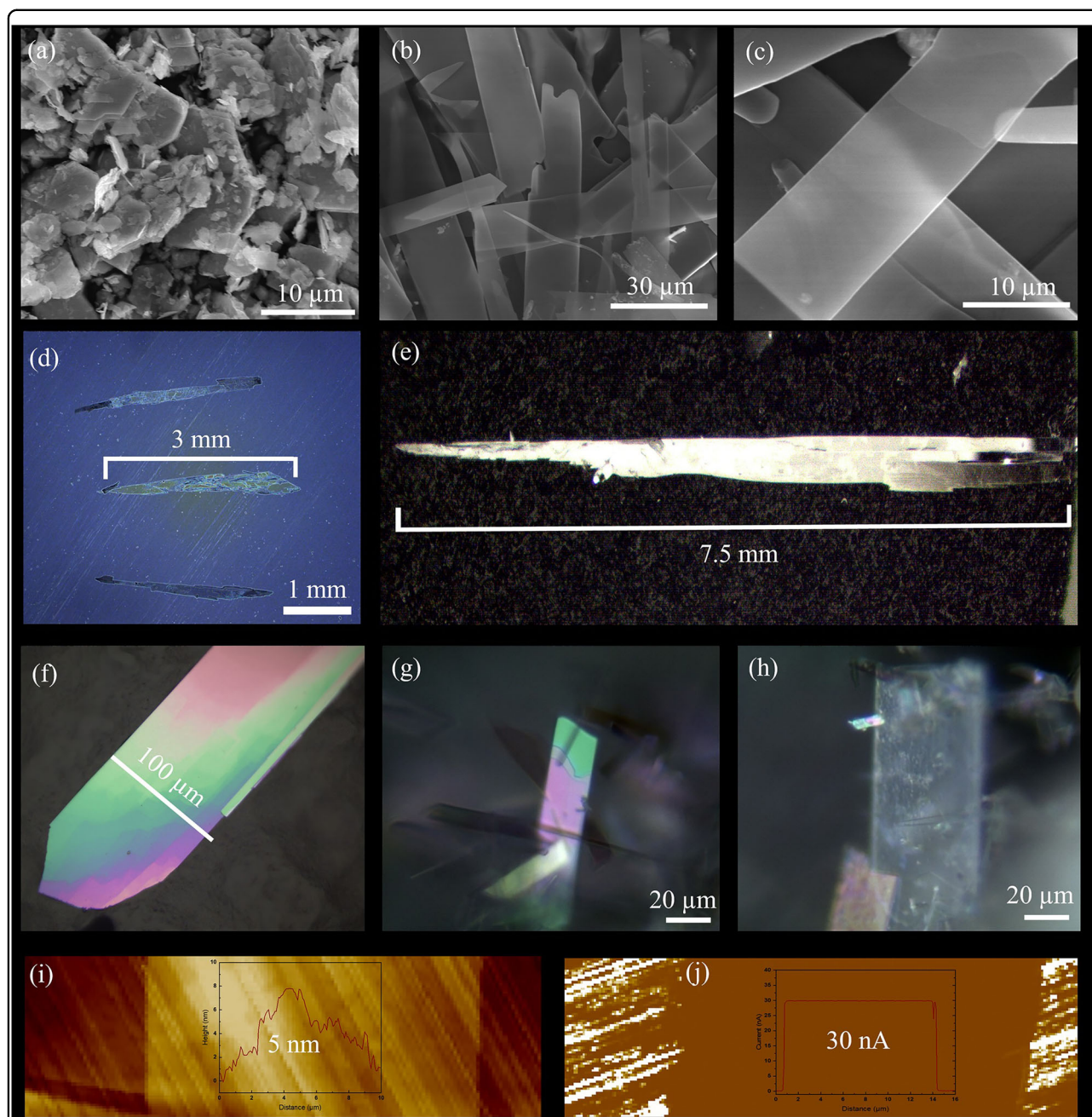
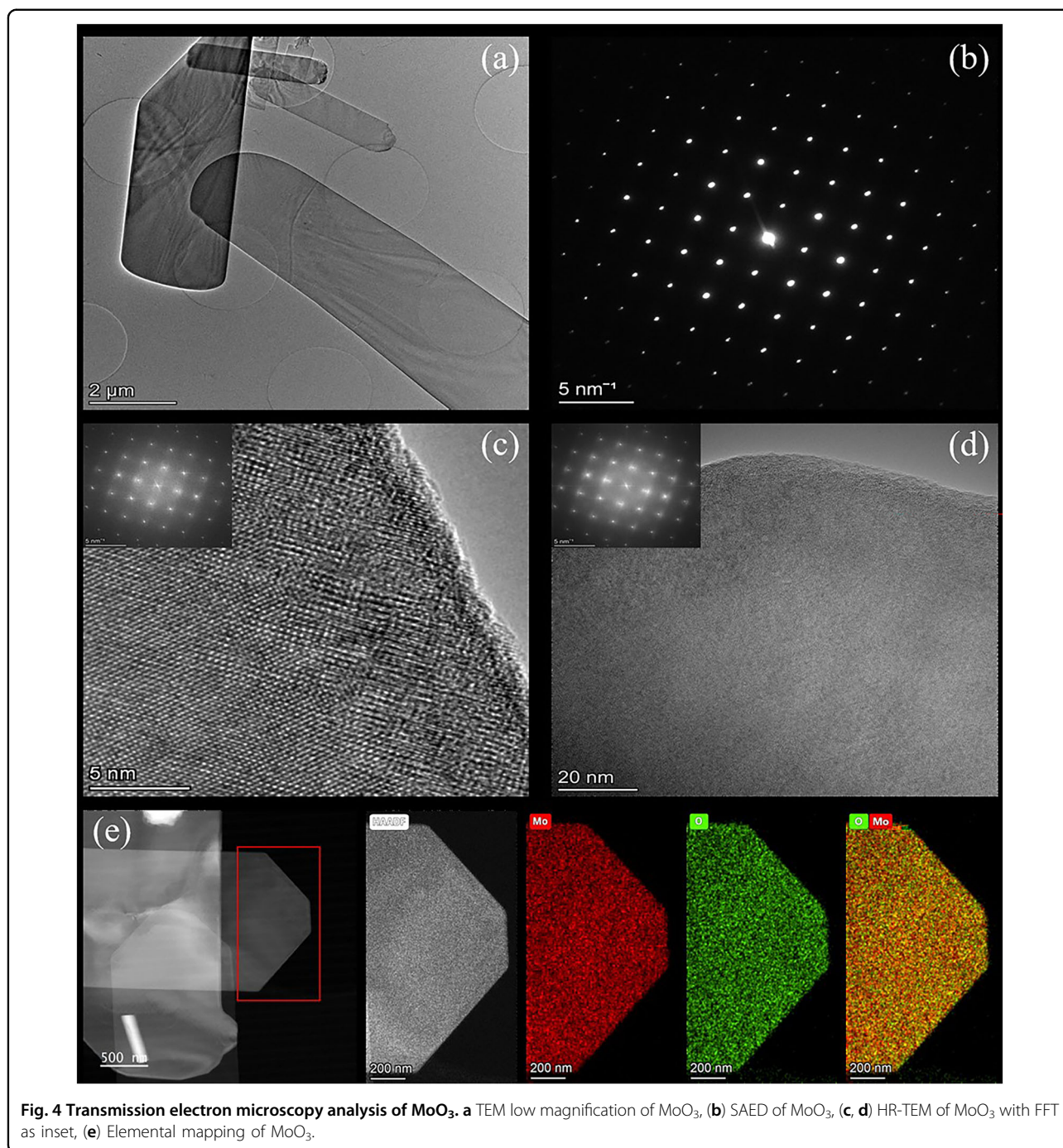


**Fig. 3 Morphological and optical characterization of  $\text{MoS}_2$  and  $\alpha\text{-MoO}_3$  crystals.** SEM Images of (a)  $\text{MoS}_2$ , (b, c)  $\text{MoO}_3$  of different magnifications. d, e Optical microscope images Demonstrating the macroscopic scale of the synthesized  $\alpha\text{-MoO}_3$  crystals (f–h) Optical images showcasing the crystal nature and the reflection of white light if the OM. i AFM topography of low-thickness  $\text{MoO}_3$  crystal. j Conductive-AFM of the same crystal.

properties of the samples. As depicted in Fig. 4e, Elemental analysis mapping offers a powerful visualization of the  $\alpha\text{-MoO}_3$  sample's homogeneity. This technique reveals a uniform distribution of elements throughout the material, signifying the absence of sulfur or other impurities. This observation strongly supports the high purity of the synthesized  $\alpha\text{-MoO}_3$ . STEM-EELS (Fig. 5) reveals

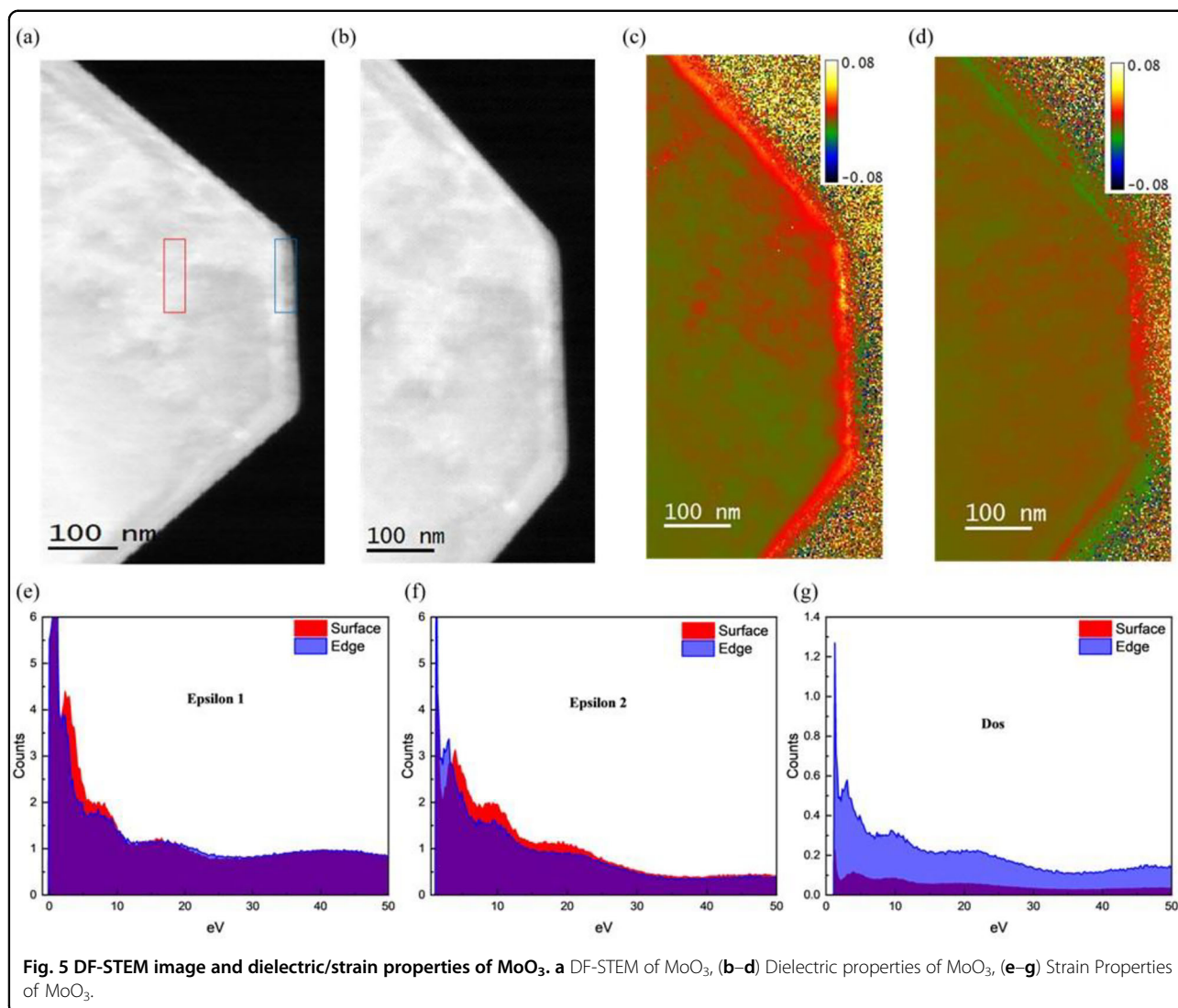
the dielectric properties of synthesized samples. Figure 5c, d shows the real and imaginary parts of the dielectric function, which have been obtained from the bulk and surface regions of a particle shown by the dark-field STEM (DF-STEM) image in Fig. 5a, b. Kramer–Kronig analysis (KKA) of the energy loss function (ELF) from bulk and surface regions (Fig. 6b–d) showed a significant



enhancement in the density of states (DOS) at the surface in the visible light range. This suggests increased visible light absorption at the surface, potentially due to surface strain.

surface regions. The results revealed a significant enhancement in the surface-region DOS in the visible light range of energies compared to the bulk region's DOS. These results imply that the surface regions of the particles absorb more energy in the visible light range

than the bulk. The enhancement in DOS at the surface regions can be linked to the presence of strain in these regions, as shown in the strain analysis of the particles, presented in Fig. 5e–g, showing a normal strain in the surface regions, which may be correlated with the enhanced surface DOS and altered dielectric properties. The FTIR spectrum shown in Supplementary Fig. 9a further confirmed the  $\alpha\text{-MoO}_3$  phase. The peaks are primarily located below  $14,000\text{ cm}^{-1}$  on the low-energy



side of the spectrum. The peak at  $989\text{ cm}^{-1}$  for the  $\alpha$ -MoO<sub>3</sub> sample is attributed to the terminal Mo=O stretching vibration, indicating the layered orthorhombic  $\alpha$ -MoO<sub>3</sub> phase<sup>49,50</sup>. A strong peak at  $815\text{ cm}^{-1}$  is assigned to the stretching vibrations of the O<sub>(3)</sub> atoms in the Mo-O-Mo units in the orthorhombic  $\alpha$ -MoO<sub>3</sub> structure<sup>51</sup>. The band at  $563\text{ cm}^{-1}$  is due to the bending vibrations of the oxygen atom (O<sub>(2)</sub>) linked to three metal atoms  $\nu(\text{O}-3\text{Mo})$  for the  $\alpha$ -MoO<sub>3</sub> sample<sup>52</sup>. Additionally, a peak around  $470\text{ cm}^{-1}$  could not be detected due to instrumental limitations, but it is thought to be due to the stretching mode of the terminal Mo-O bond<sup>53,54</sup>. The absence of other significant peaks like  $3400\text{ cm}^{-1}$  for water molecules further confirms the high purity of the  $\alpha$ -MoO<sub>3</sub> sample. Thermogravimetric analysis (TGA) was performed to investigate the  $\alpha$ -MoO<sub>3</sub> sample's thermal stability (Supplementary Fig. 9b). The results demonstrate remarkable thermal stability up to  $700\text{ }^\circ\text{C}$ , indicating their

robustness for high-temperature applications. The TGA curve shows no significant decomposition stages up to this point. However, at around  $790\text{ }^\circ\text{C}$ , there is a dramatic % weight loss of about 40%, resulting from the sublimation of MoO<sub>3</sub><sup>55</sup>.

#### This work vs state-of-the-art techniques

Molybdenum is naturally found with other elements, including several molybdenum-bearing minerals. However, the one with the most commercial significance is molybdenite (MoS<sub>2</sub>), a natural mineral form of molybdenum disulfide<sup>56,57</sup>.

The flowchart presented in Fig. 6 illustrates the streamlined synthesis processes of our novel microwave method compared to SOTA. Both approaches share the same initial four stages—crushing, grinding, flotation, and leaching—from the mined molybdenum ore to molybdenite (MoS<sub>2</sub>) formation. As described in detail in the

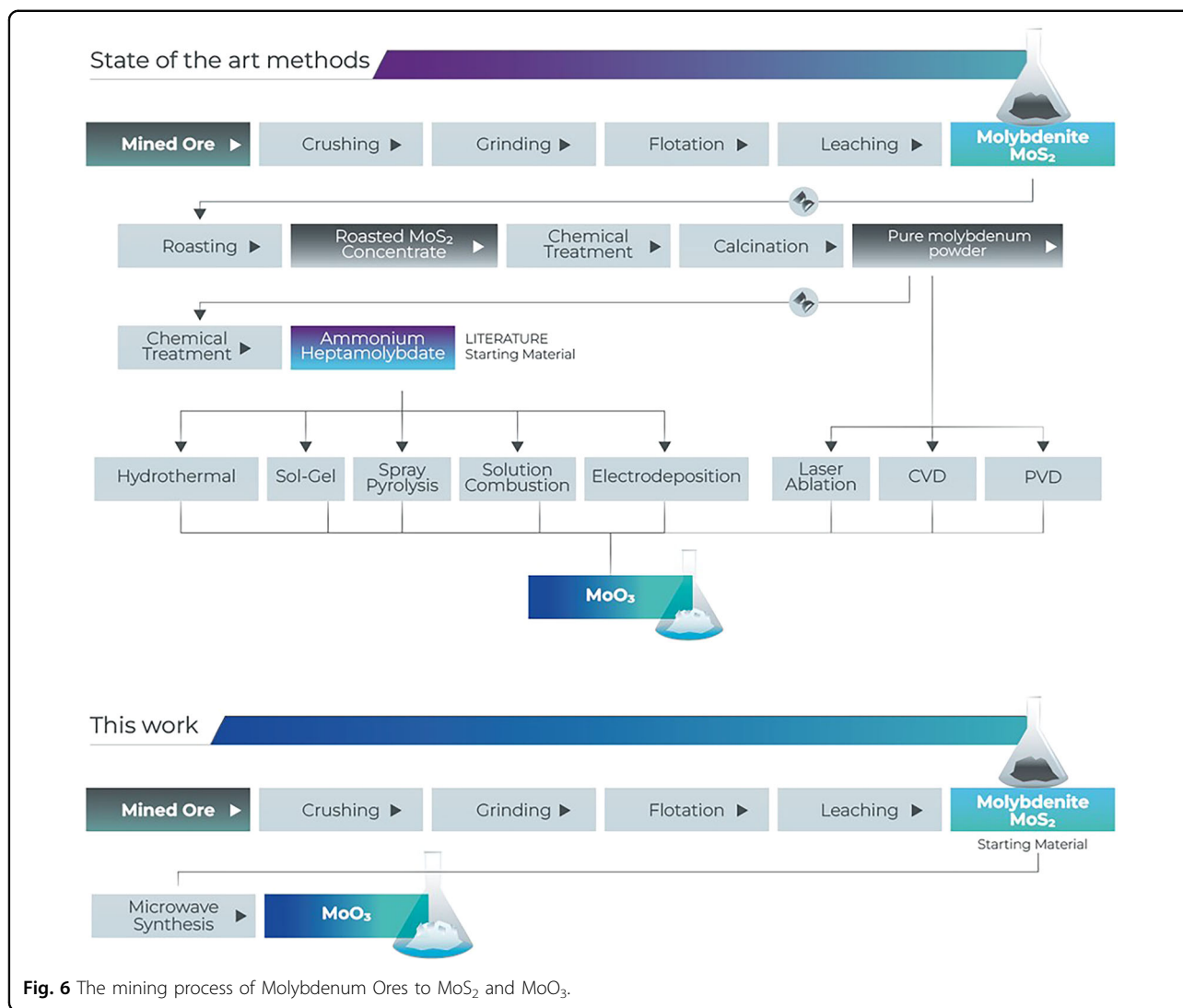
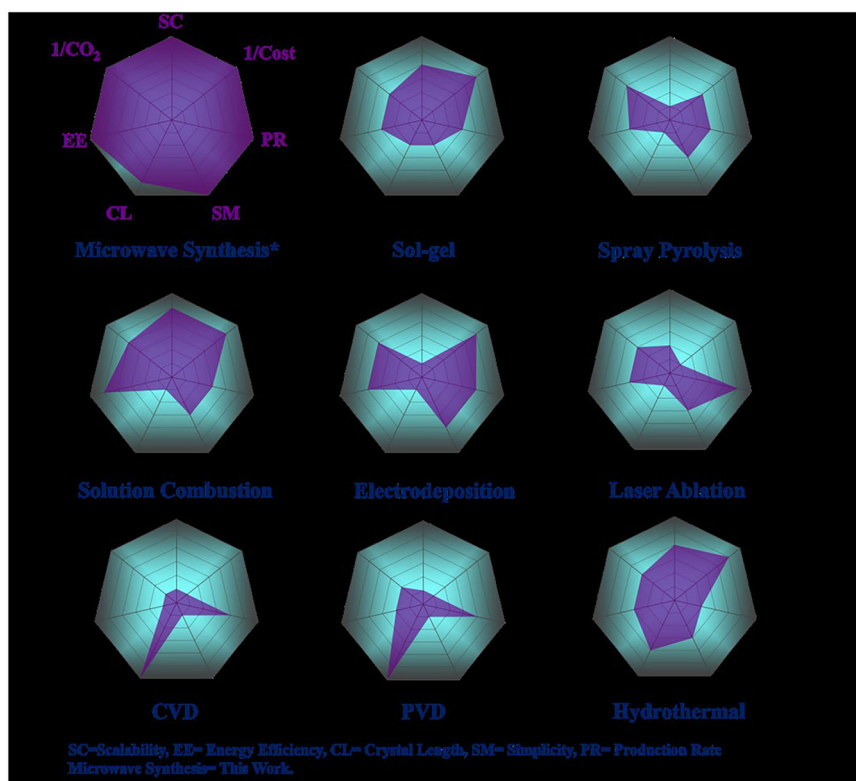


Fig. 6 The mining process of Molybdenum Ores to MoS<sub>2</sub> and MoO<sub>3</sub>.

supporting information file, these processes are crucial for extracting and purifying molybdenite, but there is no variation between the methods in these preliminary steps<sup>58–61</sup>. The key distinction between the two approaches emerges after molybdenite (MoS<sub>2</sub>) is formed. In this work, molybdenite is directly used as the starting material without requiring additional processing. In contrast, in conventional SOTA methods, multiple subsequent processes are required for MoO<sub>3</sub> crystals synthesis. Specifically, molybdenite is roasted at high temperatures (around 500 °C)<sup>61</sup>, followed by chemical treatments and calcination to produce pure molybdenum powder<sup>62</sup>. This purified molybdenum is the starting material for various synthesis techniques such as CVD, PVD, and laser ablation. After roasting, further chemical treatments are applied to convert the molybdenite into ammonium heptamolybdate (AHM), the starting material for other commonly used SOTA methods. The takeaway from

Fig. 6 is that this work offers an alternative approach to synthesizing MoO<sub>3</sub> crystals by bypassing additional steps and intermediate compounds. Directly utilizing molybdenite as the starting material and employing microwave synthesis eliminates energy-intensive processes such as roasting (500 °C)<sup>63,64</sup>, chemical treatments, and calcination at temperatures ranging from 500–1000 °C. The exclusion of these cumbersome processes significantly streamlines the synthesis route, giving this work a distinct advantage over conventional techniques. Figure 7 quantitatively compares our microwave synthesis with eight common SOTA methods across seven key Criteria: Scalability (SC), Crystal Length (CL), Production Rate (PR), Energy efficiency (EE), Simplicity (SM), (1/CO<sub>2</sub>), which is kilograms of CO<sub>2</sub> emissions equivalent. Data were collected through analysis of Supplementary Table 3 for (CL, PR, SM, SC, and 1/Cost), and by conducting Life Cycle Assessment (LCA) using SimaPro for (EE and



**Fig. 7 Comparison between this work and the eight most common methods.** (Hydrothermal[S9-S95], Spray Pyrolysis[S96- S114], Laser Ablation[S115- S122], Sol-gel[S123- S131], Solution Combustion[S132-S139], Electrodeposition[S140-S146], PVD[S147-S162], and CVD[S163-S175]).

1/CO<sub>2</sub>). It is a standard unit used to quantify the impact of different greenhouse gases (GHGs) on climate change in terms of the equivalent amount of carbon dioxide (CO<sub>2</sub>) that would have the same global warming potential (GWP) (Supplementary Fig. 17) and, (1/Cost) is a cost calculation for the machinery involved into making MoO<sub>3</sub> crystals for each method.

When comparing methods based on energy efficiency -measured by the electricity consumed to produce 1 g of MoO<sub>3</sub> in kWh- Microwave Synthesis is the most energy-efficient, consuming only 0.5 kWh. Solution combustion consumes around 4 kWh, while Electrodeposition uses about 19 kWh. Spray pyrolysis requires approximately 15 kWh. Sol-gel and laser ablation each consumes around 30kWh.

Hydrothermal processes need about 35 kWh. CVD and PVD are the least energy-efficient, consuming 70 and 60 kWh, respectively. The production rates for each method were approximately as follows: microwave synthesis was 10 min, which is the least time consumed to produce MoO<sub>3</sub> crystals among SOTA methods. Meanwhile, hydrothermal ranged from 8 to 20 h, with an average of 12 h being the most common duration. Spray pyrolysis averaged 30 min for spraying and 1 h for evaporation. Electrodeposition required a couple of minutes

for deposition and an additional 2 h for annealing. Sol-gel needed around 10 h for gel formation and subsequent calcination. Solution combustion took a couple of minutes to mix and approximately 1 h for combustion. Laser Ablation averaged 30 min for irradiation of the molybdenum target. CVD and PVD required around 3 h to reach the desired temperature, maintain it, and then evacuate to collect the product. Scalability, measured by the time needed to produce 1 g of MoO<sub>3</sub>, is another crucial criteria. For this criteria, the Microwave Synthesis method needed only 1 h to produce 1 gram of MoO<sub>3</sub>, which offers a potentially scalable approach to produce MoO<sub>3</sub> crystals. Solution Combustion required around 2.5 h. The Sol-gel method and hydrothermal processes each needed around 20 to 25 h. CVD and PVD methods required 20 to 30 h to produce 1 gram. For techniques like laser ablation, spray pyrolysis, and electroplating, typically used to create thin films, scalability was assessed by the time required to produce milligrams per square centimeter. It was determined that to make 1 gram of MoO<sub>3</sub>, electroplating would take around 80 h, laser ablation would take about 300 h, and spray pyrolysis would take approximately 600 h. These high times are reasonable given that these methods are not typically used for large-scale production but for creating thin films on

substrates. Simplicity is another essential criteria, evaluated based on the number of steps in the process, the complexity of the machinery involved, the number of chemicals used, and how easy these chemicals are to handle. Microwave Synthesis is a simple and easy method that requires only a microwave. Solution combustion also scores high on simplicity, needing minimal chemicals and machinery, as it only involves burning the chemicals. Electrodeposition and spray pyrolysis require fewer chemicals but involve handling specific machinery like a potentiostat and spray nebulizer. Hydrothermal and Sol-gel methods are relatively easy to handle but require a moderate amount of chemicals to initiate the reaction. Laser Ablation is more complex, involving complex machinery and numerous safety concerns. CVD and PVD are the most complicated, requiring many steps and handling a sensitive and controlled environment. The cost calculations are based on the machinery cost and energy consumed during the process. Microwave Synthesis emerged as the most cost-effective method. Solution Combustion followed, ranging from 500 to 1000 USD, while the Sol-gel method ranged between 1000 to 2000 USD. Electrodeposition methods fell within the range of 1500 to 2500 USD. Hydrothermal processes cost between 500 and 1000 USD, whereas spray pyrolysis ranges from 10,000 to 25,000 USD. Laser Ablation method is significantly more costly, ranging between 10,000 to 100,000 USD. CVD and PVD methods were the most expensive, with machinery costs ranging from 100,000 to 250,000 USD. These cost assessments provide insights into the financial feasibility of each method, influencing their practicality and adoption in various applications. The final criteria crystal length is determined by SEM images from the references, and distinct averages emerge. Hydrothermal processes exhibit an average of several micrometers to 200 micrometers, while sol-gel and solution combustion methods typically result in crystal lengths in the range of several micrometers. Electrodeposition, spray pyrolysis, and Laser ablation produce crystals measured in nanometers, whereas CVD and PVD methods yield the longest crystals, with PVD achieving lengths of up to a few mm to cm. In terms of crystal length, Microwave Synthesis can reach up to 7 mm, comparable to other advanced methods like CVD and PVD; being compared to CVD and PVD in crystal synthesis is an advantage, making it a viable alternative without going through the complexity of these methods. To demonstrate the electrical properties and practical utility of the synthesized  $\alpha$ - $\text{MoO}_3$  crystals, we fabricated and characterized Metal-Interlayer-Oxide-Semiconductor (MIOS) memristive devices.

#### Application for alpha molybdenum trioxide

$\text{MoO}_3$  has been investigated as a compelling active material for various memristive devices due to its diverse

redox states and tunable oxygen vacancy concentrations<sup>65–68</sup>. In this section, we demonstrate an enhanced memristive effect in a  $\text{Si}/\text{MoO}_3/\text{Al}_2\text{O}_3/\text{Cu}$  structure (details in the Experimental Section), leveraging the structural and electrical properties of the synthesized  $\text{MoO}_3$  crystals. Figure 8 illustrates the fabricated MIOS device structure: (a) Top-view optical micrograph showing a device with a  $\sim 623$  nm thick  $\text{MoO}_3$  crystal. (b) Schematic cross-sectional diagram of the device stack ( $\text{Si}/\text{MoO}_3/\text{Al}_2\text{O}_3/\text{Cu}$ ), and (c) AFM topography of the  $\text{MoO}_3$  crystal surface after  $\text{Al}_2\text{O}_3$  and Cu deposition, confirming the crystal's morphology is preserved during device fabrication. Electrical characterization (details in Experimental Section) of the fabricated MIOS devices reveal clear and robust bipolar resistive switching, as evidenced by the current-voltage ( $I$ - $V$ ) characteristics in Fig. 9a, which is expected in Transition Metal Oxides (TMO)-based memristors. Notably, Our MIOS devices incorporating the  $\alpha$ - $\text{MoO}_3$  exhibited remarkably low SET ( $\sim -2$  V) and RESET ( $\sim 2$  V) voltages even with a relatively thick ( $\sim 623$  nm)  $\text{MoO}_3$  crystal. This low voltage operation is a significant advantage for energy-efficient memory applications and is not typically observed in  $\text{MoO}_3$  memristors of this thickness. Control devices fabricated without a  $\text{MoO}_3$  layer ( $p++$   $\text{Si}/\text{Al}_2\text{O}_3/\text{Cu}$ ) showed significantly inferior memristive performance, exhibiting higher switching voltages, smaller switching windows, and a low resistance state (LRS), highlighting the crucial role of the  $\text{MoO}_3$  crystals. Detailed inspection of the  $I$ - $V$  log-log plots in Fig. 9b shows the charge transport mechanisms governing the resistive switching. In the LRS, the  $I$ - $V$  curves show a linear ohmic relationship with a slope close to unity ( $|I| \propto |V|^\alpha$ ,  $\alpha \approx 1.06$  in negative bias and  $\alpha \approx 1.05$  in positive bias). This ohmic behavior in the LRS leads to an increased concentration of mobile oxygen vacancies acting as donors at the  $\text{Al}_2\text{O}_3/\text{MoO}_3$  interface<sup>66,67</sup>. On the other hand, in the high resistance state (HRS), especially under positive bias (after RESET), the  $I$ - $V$  characteristics deviate from linearity, showing a slope of approximately 1.8 ( $|I| \propto |V|^{1.8}$ ). This non-linear space-charge-limited current (SCLC) and trapped-charge-limited current (TCLC) in HRS suggests that the current is limited by space charge effects and available trap states within the  $\text{MoO}_3$ , resulting from a reduced carrier concentration after the Forming and follow-up RESET processes<sup>68</sup>. This transition from ohmic conduction in the LRS to SCLC in the HRS supports a non-filamentary, interfacial switching mechanism<sup>69,70</sup>, where the barrier at the  $\text{MoO}_3/\text{Al}_2\text{O}_3$  interface is dynamically modulated<sup>66,71</sup>. Moreover, we propose that this modulation arises from the field-assisted migration of oxygen vacancies within the  $\text{MoO}_3$  crystal (Fig. 9d)<sup>6,7</sup>. Since pristine  $\alpha$ - $\text{MoO}_3$  crystals possess low intrinsic oxygen vacancy concentrations, an initial electroforming step (Supplementary Figs. 13–15) was crucial

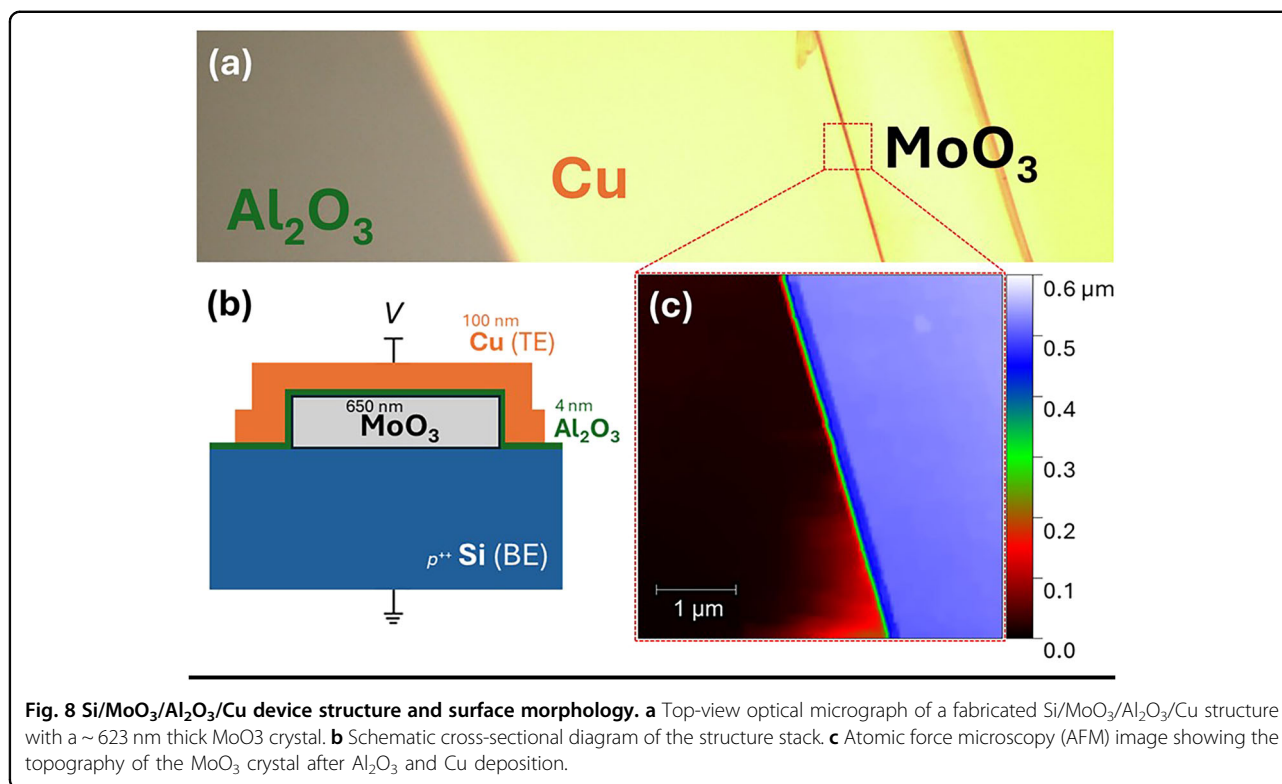


**Fig. 8** Si/MoO<sub>3</sub>/Al<sub>2</sub>O<sub>3</sub>/Cu device structure and surface morphology. **a** Top-view optical micrograph of a fabricated Si/MoO<sub>3</sub>/Al<sub>2</sub>O<sub>3</sub>/Cu structure with a ~623 nm thick MoO<sub>3</sub> crystal. **b** Schematic cross-sectional diagram of the structure stack. **c** Atomic force microscopy (AFM) image showing the topography of the MoO<sub>3</sub> crystal after Al<sub>2</sub>O<sub>3</sub> and Cu deposition.

to generate and optimally localize the necessary oxygen vacancies at the Al<sub>2</sub>O<sub>3</sub>/MoO<sub>3</sub> interface. This electroforming process electrochemically reduces Mo<sup>6+</sup> ions, creating mobile oxygen vacancies and facilitating subsequent redox reactions at optimal sites along the crystal interface during SET and RESET operations<sup>72</sup>. Endurance testing (Fig. 9c) demonstrates stable and repeatable bipolar switching over 33 cycles (for a device with a ~511 nm thick MoO<sub>3</sub> crystal), with minimal degradation in the on/off ratio and switching voltages. The inset of Fig. 9c shows the voltage pulse train used for the measurements with 2 ms pulse durations. The proposed switching mechanism is illustrated via energy band diagrams in Fig. 9d, showing the electric field-induced drift and diffusion of these generated oxygen vacancies during the forming process within the MoO<sub>3</sub> layer. During SET (negative bias), oxygen vacancies migrate towards the Al<sub>2</sub>O<sub>3</sub> interface, forming localized conductive regions responsible for the high resistance state. During RESET (positive bias), oxygen vacancies move away, rupturing these regions and restoring the high resistance state. The Al<sub>2</sub>O<sub>3</sub> layer acts as a crucial interface, controlling the nucleation and localization of these conductive regions and contributing to the observed low-voltage operation<sup>71,73</sup>.

The low SET and RESET voltages achieved in our MoO<sub>3</sub>-based structures, despite the substantial MoO<sub>3</sub> thickness, represent a notable advancement. While MoO<sub>3</sub>

has been extensively explored for resistive switching<sup>72,74,75</sup>, achieving such low voltage operation in devices with easily synthesized, hundreds of nanometers thick MoO<sub>3</sub> crystals are unconventional and desirable for low-power memory applications. Compared to the Al<sub>2</sub>O<sub>3</sub>-based structures, which often rely on charge trapping or tunneling mechanisms<sup>76</sup>, our MoO<sub>3</sub> devices exhibit bipolar resistive switching indicative of ionic migration, offering a distinct operational pattern with potentially superior endurance characteristics after further optimization. Supplementary Table S4 benchmarks our devices against reported MoO<sub>3</sub> and other high-k oxide-based memristors. Despite a much thicker switching layer, our operating voltages are lower than those for sputtered and CVD MoO<sub>3</sub> [S178, S180, S181, S183] and comparable to solution-processed MoO<sub>3</sub> [S176]. The devices also show ON/OFF current ratios and endurance similar to reported MoO<sub>3</sub> [S176] and Al<sub>2</sub>O<sub>3</sub> [S181] memristors, highlighting the excellent performance achieved with our microwave-synthesized MoO<sub>3</sub> crystals. This performance enhancement underscores the potential of utilizing high-quality MoO<sub>3</sub> crystals with a proper tunnel barrier to realize more reliable, cost- and energy-efficient memristive switching. Future research should focus on in-situ spectroscopic investigations (e.g., XPS, TEM-EELS) to directly characterize the oxygen vacancy dynamics and Mo oxidation state changes at the Al<sub>2</sub>O<sub>3</sub>/MoO<sub>3</sub> interface during resistive switching. Further systematic optimization of the Al<sub>2</sub>O<sub>3</sub> interface (e.g., thickness

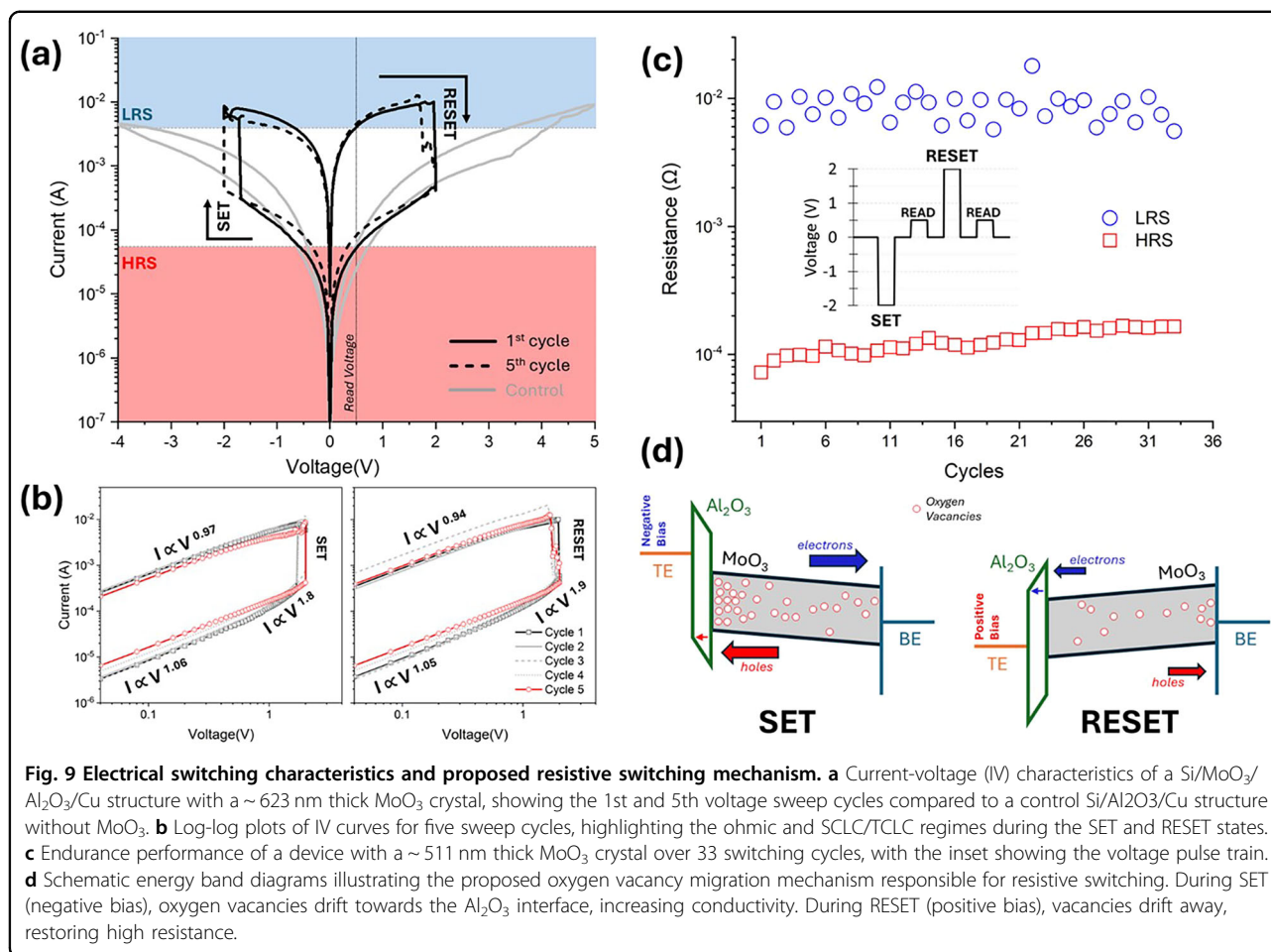


**Fig. 9** Electrical switching characteristics and proposed resistive switching mechanism. **a** Current-voltage (IV) characteristics of a Si/MoO<sub>3</sub>/Al<sub>2</sub>O<sub>3</sub>/Cu structure with a ~623 nm thick MoO<sub>3</sub> crystal, showing the 1st and 5th voltage sweep cycles compared to a control Si/Al<sub>2</sub>O<sub>3</sub>/Cu structure without MoO<sub>3</sub>. **b** Log-log plots of IV curves for five sweep cycles, highlighting the ohmic and SCLC/TCLC regimes during the SET and RESET states. **c** Endurance performance of a device with a ~511 nm thick MoO<sub>3</sub> crystal over 33 switching cycles, with the inset showing the voltage pulse train. **d** Schematic energy band diagrams illustrating the proposed oxygen vacancy migration mechanism responsible for resistive switching. During SET (negative bias), oxygen vacancies drift towards the Al<sub>2</sub>O<sub>3</sub> interface, increasing conductivity. During RESET (positive bias), vacancies drift away, restoring high resistance.

variation, exploring alternative high-k dielectrics like HfO<sub>2</sub> or TiO<sub>2</sub>) could lead to even greater improvements in device performance, potentially unlocking the potential of these devices for emerging applications in energy-efficient neuromorphic computing and advanced in-sensor processing technologies<sup>77,78</sup>.

## Conclusion

In summary, this work demonstrates microwave synthesis as a remarkably efficient and eco-friendly approach for producing high-quality metal oxides, exemplified by synthesizing crystalline  $\alpha$ -MoO<sub>3</sub>. Compared to state-of-the-art methods, our approach offers significant advantages in simplicity, production rate (achieving MoO<sub>3</sub> crystals in just 2 min, ~50–600x faster), scalability (1 g/h, 2.5–600x better), energy efficiency (0.5 kWh/g, 8–140x better), and reduced CO<sub>2</sub> emissions (~10–150x less). The resulting  $\alpha$ -MoO<sub>3</sub> exhibits long crystals up to 8 mm in length, compared to complex processes such as CVD and PVD, showcasing the potential of microwave synthesis in achieving high-quality materials with desirable properties. Furthermore, we have

shown that integrating these high-quality MoO<sub>3</sub> crystals with an Al<sub>2</sub>O<sub>3</sub> barrier in MIOS structures enables stable, low-voltage bipolar switching driven by oxygen vacancy dynamics. Finally, this microwave synthesis method, combined with the demonstrated memristor performance, positions  $\alpha$ -MoO<sub>3</sub> as a promising material for energy-efficient next-generation memory and neuromorphic computing applications.

## Experimental section

### Chemicals and reagents

MoS<sub>2</sub> powder (average size of less than 5  $\mu$ m), and isopropyl alcohol (C<sub>3</sub>H<sub>8</sub>O, 99%) were purchased from Sigma-Aldrich. All the chemicals used in the experiments were used without further purification.

### Characterization and measurements

Samples were irradiated in a microwave (1000 watts) and 2.45 GHz. The crystallinity of the samples was measured using X-ray diffraction (XRD Bruker D2 phaser). Raman analysis of the starting materials and the exfoliated samples were performed by Renishaw spectrometer using

532 nm laser (2.33 eV) excitation and 50x objective lens. The laser power was kept below 1 mW to prevent sample damage. 20 spectra were recorded (each one at a different location) for each sample to create statistical data for the samples. Morphology of the samples was done by scanning electron microscopy ((SEM) Nova NanoSEM 650, beam resolution 0.8 nm). XPS spectra were recorded using a Thermo Scientific K-Alpha spectrometer. Samples were analyzed at the nanoscale using a TEM of model Titan ThemisZ equipped with double aberration correctors, high-throughput X-ray energy dispersive spectroscopy (EDS), and electron energy loss spectroscopy (EELS) detectors. The analysis was carried out by operating the microscope at an accelerating voltage of 300 kV. The morphology of the samples was analyzed using bright-field TEM (BF-TEM). The structure was investigated using selected area electron diffraction (SAED) and high-resolution TEM (HRTEM). Whereas the elemental composition of the samples was determined using EDS in TEM mode. Moreover, the elemental composition maps or distributions were generated by processing the EDS datasets acquired in synchronized scanning transmission electron microscopy (STEM) mode. The samples' dielectric properties and density of states (DOS) were probed using the low-loss EELS, also in the STEM mode. The presence of strain at the edges or surface of the samples was investigated by carrying out the four-dimensional hyperspectral datasets acquired in synchronization of STEM mode and micro-diffraction mode, labeled as the 4DSTEM technique. The elemental composition and the corresponding elemental maps were acquired and processed in ThermoFisher Software called Velox v2.05. Whereas the rest of the TEM analysis-related datasets were acquired and subsequently processed in Gatan Microscopy Suite (GMS) of version 3.5 from Gatan, Inc. TGA analysis was done using STA 449 F5 Jupiter. UV-Vis was done using specord 50 plus. FTIR was done using NiCOLET iS50. UV-vis spectroscopic data was obtained using an Oca Insight DH-2000 spectrometer utilizing a deuterium lamp. The absorption and transmission spectra were recorded in the 180–600 nm wavelength range. The integration time was set to automatic, and an average of 20 spectra was obtained.

MIOS devices were fully fabricated in a class 1000 cleanroom, and fabrication started with transferring the MoO<sub>3</sub> crystals onto cleaned and O<sub>2</sub> plasma-treated p + + silicon (0.002–0.003 Ω.cm) substrates using a PDMS stamp to maintain their structural integrity. Subsequently, a 4 nm thick Al<sub>2</sub>O<sub>3</sub> layer was deposited via atomic layer deposition (ALD) as a uniform, high-k oxide, pinhole-free barrier. Finally, a 100 nm thick Cu top electrode (TE) was thermally evaporated and patterned through a shadow mask carefully aligned over the MoO<sub>3</sub> crystals.

Electrical characterizations were conducted using a probe station and parameter analyzer under ambient conditions in a dark box, with the p + + Si substrate serving as the grounded bottom electrode (BE) and a gold-coated tungsten probe applying bias to Cu TE.

#### Acknowledgements

This work was supported by Khalifa University of Science and Technology under the project FSU-2023-010, 2D Materials for Space Applications. The authors gratefully acknowledge the financial and technical support provided by Khalifa University, as well as the facilities and resources made available by the Advanced Research and Innovation Center (ARIC), Research and Innovation Center for 2D Materials (RIC-2D) and INTRATOMIC. The authors thank the King Abdulla University of Science and Technology (KAUST) CoreLab facilities for allowing them to use electron microscopes to carry out the presented TEM analysis.

#### Author details

<sup>1</sup>Department of Aerospace Engineering, Khalifa University of Science and Technology, Abu Dhabi, United Arab Emirates. <sup>2</sup>Department of Electrical Engineering, Khalifa University of Science and Technology, Abu Dhabi, United Arab Emirates. <sup>3</sup>Department of Physics, Khalifa University of Science and Technology, Abu Dhabi, United Arab Emirates. <sup>4</sup>Department of Mechanical Engineering, Khalifa University of Science and Technology, Abu Dhabi, United Arab Emirates. <sup>5</sup>Cambridge Graphene Center, University of Cambridge, Cambridge, UK

#### Author contributions

R.E. and Y.A. contributed to the conceptualization and experimental design. R.E., S.S., I.A., and D.A. were responsible for the experimental fabrication and characterization of the materials. A.R. and A.N. were responsible for fabricating and analyzing the device. R.E., Y.A., H.B., and A.N. performed the formal analysis and data curation. R.E. wrote the original manuscript. Y.A., A.N., and H.B. supervised this study, including the revisions. Y.A. was responsible for acquiring the funds. All authors have read and agreed to the published version of the manuscript.

#### Competing interests

A provisional patent application directed to this technology (63/571,840) has been filed by Khalifa University, but it is currently unlicensed. The inventors listed are Rami Elkaffas, Fahad Al Absi, and Yarjan Abdul Samad. The other authors declare no competing interests.

#### Ethics approval and consent to participate

All methods were performed in accordance with the relevant guidelines and regulations. This study did not involve human participants, personal data, human tissue, or live vertebrate animals. Accordingly, approval from a human research ethics committee or an animal ethics committee was not required under institutional and national regulations. As no human participants were involved, informed consent to participate was not required.

#### Use of large language model (ChatGPT)

The authors used ChatGPT to rephrase and correct spelling and grammar errors to ensure a clearer depiction of the work. The authors ensured that the final manuscript agreed with the technical and scientific knowledge.

#### Publisher's note

Springer Nature remains neutral with regard to jurisdictional claims in published maps and institutional affiliations.

**Supplementary information** The online version contains supplementary material available at <https://doi.org/10.1038/s41427-026-00637-8>.

Received: 10 June 2025 Revised: 22 October 2025 Accepted: 3 February 2026

Published online: 24 March 2026

## References

- Ruta, F. L. et al. Surface plasmons induce topological transition in graphene/ $\alpha$ -MoO<sub>3</sub> heterostructures. *Nat. Commun.* **13**, 3719, <https://doi.org/10.1038/s41467-022-31477-z> (2022).
- Zhang, Q. et al. Unidirectionally excited phonon polaritons in high-symmetry orthorhombic crystals. *Sci. Adv.* **8**, eabn9774, <https://doi.org/10.1126/sciadv.abn9774> (2022).
- Choi, D. K. et al. Highly efficient, heat dissipating, stretchable organic light-emitting diodes based on a MoO<sub>3</sub>/Au/MoO<sub>3</sub> electrode with encapsulation. *Nat. Commun.* **12**, 2864, <https://doi.org/10.1038/s41467-021-23203-y> (2021).
- Cong, S. et al. Diverse adsorption/desorption abilities originating from the nanostructural morphology of VOC gas sensing devices based on molybdenum trioxide nanorod arrays. *Adv. Mater. Interfaces* **3**, 1600252, <https://doi.org/10.1002/admi.201600252> (2016).
- Puebla, S. et al. Strain tuning MoO<sub>3</sub> vibrational and electronic properties. *Npj 2D Mater. Appl.* **8**, 1–9, <https://doi.org/10.1038/s41699-024-00442-3> (2024).
- Imtiaz, S. et al. Electrocatalysis on separator modified by molybdenum trioxide nanobelts for lithium–sulfur batteries. *Adv. Mater. Interfaces* **5**, 1800243, <https://doi.org/10.1002/admi.201800243> (2018).
- Martinez-Garcia, A. et al. High rate and durable, binder free anode based on silicon loaded MoO<sub>3</sub> nanoplatelets. *Sci. Rep.* **5**, 10530, <https://doi.org/10.1038/srep10530> (2015).
- Li, S., Shao, C., Liu, Y., Tang, S. & Mu, R. Nanofibers and nanoplatelets of MoO<sub>3</sub> via an electrospinning technique. *J. Phys. Chem. Solids* **67**, 1869–1872, <https://doi.org/10.1016/j.jpcs.2006.04.017> (2006).
- Huang, L. et al. Three-dimensional MoO<sub>3</sub> nanoflowers assembled with nanosheets for rhodamine B degradation under visible light. *Mater. Res. Bull.* **108**, 38–45, <https://doi.org/10.1016/j.materresbull.2018.08.036> (2018).
- Zhao, D. et al. Facile synthesis of MoO<sub>3</sub> nanospheres and their application in water treatment. *Mater. Lett.* **256**, 126648, <https://doi.org/10.1016/j.matlet.2019.126648> (2019).
- Yan, B. et al. Orientation controllable growth of MoO<sub>3</sub> nanoflakes: micro-Raman, field emission, and birefringence properties. *J. Phys. Chem. C* **113**, 20259–20263, <https://doi.org/10.1021/jp907602w> (2009).
- Scanlon, D. O. et al. Theoretical and experimental study of the electronic structures of MoO<sub>3</sub> and MoO<sub>2</sub>. *J. Phys. Chem. C* **114**, 4636–4645, <https://doi.org/10.1021/jp9093172> (2010).
- Qu, Q., Zhang, W.-B., Huang, K. & Chen, H.-M. Electronic structure, optical properties and band edges of layered MoO<sub>3</sub>: a first-principles investigation. *Comput. Mater. Sci.* **130**, 242–248, <https://doi.org/10.1016/j.commatsci.2017.01.014> (2017).
- Andron, I. et al. Photochromic behavior of ZnO/MoO<sub>3</sub> interfaces. *ACS Appl. Mater. Interfaces* **12**, 46972–46980, <https://doi.org/10.1021/acsami.0c13335> (2020).
- Ivanova, T., Gesheva, K. A., Popkirov, G., Ganchev, M. & Tzvetkova, E. Electrochromic properties of atmospheric CVD MoO<sub>3</sub> and MoO<sub>3</sub>–WO<sub>3</sub> films and their application in electrochromic devices. *Mater. Sci. Eng. B* **119**, 232–239, <https://doi.org/10.1016/j.mseb.2004.12.084> (2005).
- Hu, G. et al. Topological polaritons and photonic magic angles in twisted  $\alpha$ -MoO<sub>3</sub> bilayers. *Nature* **582**, 209–213, <https://doi.org/10.1038/s41586-020-2359-9> (2020).
- Morita, M. et al. Chromogenic amorphous MoO<sub>3</sub>–x nanosheets and their nanostructured films for smart window applications. *ACS Appl. Nano Mater.* **4**, 8781–8788, <https://doi.org/10.1021/acsnm.1c01428> (2021).
- Zheng, W. et al. Improvement of the thermoelectric properties of a MoO<sub>3</sub> monolayer through oxygen vacancies. *Beilstein J. Nanotechnol.* **10**, 2031–2038, <https://doi.org/10.3762/bjnano.10.199> (2019).
- Alex, K. V., Silva, J. P. B., Kamakshi, K. & Sekhar, K. C. Ternary heterostructures based on BaTiO<sub>3</sub>/MoO<sub>3</sub>/Ag for highly efficient and reusable photocatalytic applications. *Adv. Mater. Interfaces* **10**, 2201948, <https://doi.org/10.1002/admi.202201948> (2023).
- Shahzad, R. F. et al. Designing molybdenum trioxide and hard carbon architecture for stable lithium-ion battery anodes. *Adv. Mater. Interfaces* **11**, 2400258, <https://doi.org/10.1002/admi.202400258> (2024).
- Brezesinski, T., Wang, J., Tolbert, S. H. & Dunn, B. Ordered mesoporous  $\alpha$ -MoO<sub>3</sub> with iso-oriented nanocrystalline walls for thin-film pseudocapacitors. *Nat. Mater.* **9**, 146–151, <https://doi.org/10.1038/nmat2612> (2010).
- Cai, P. et al. An ultraviolet-deposited MoO<sub>3</sub> film as anode interlayer for high-performance polymer solar cells. *Adv. Mater. Interfaces* **7**, 1901912, <https://doi.org/10.1002/admi.201901912> (2020).
- Kumar, R. et al. Growth of MoS<sub>2</sub>–MoO<sub>3</sub> hybrid microflowers via controlled vapor transport process for efficient gas sensing at room temperature. *Adv. Mater. Interfaces* **5**, 1800071, <https://doi.org/10.1002/admi.201800071> (2018).
- Huang, P.-R., He, Y., Cao, C. & Lu, Z.-H. Impact of lattice distortion and electron doping on  $\alpha$ -MoO<sub>3</sub> electronic structure. *Sci. Rep.* **4**, 7131, <https://doi.org/10.1038/srep07131> (2014).
- Kedves, E.-Z. et al. Dependence of cationic dyes' adsorption upon  $\alpha$ -MoO<sub>3</sub> structural properties. *Appl. Surf. Sci.* **573**, 151584, <https://doi.org/10.1016/j.susc.2021.151584> (2022).
- Ramirez, I. J. Synthesis of h-MoO<sub>3</sub> by vacuum drying and its structural and electrochemical characterisation. *Mater. Lett.* **57**, 1034–1039 (2003).
- Mariotti, D., Lindström, H., Bose, A. C. & Ostrikov, K. (K. en). Monoclinic  $\beta$ -MoO<sub>3</sub> nanosheets produced by atmospheric microplasma: application to lithium-ion batteries. *Nanotechnology* **19**, 495302, <https://doi.org/10.1088/0957-4484/19/49/495302> (2008).
- Song, J., Ni, X., Gao, L. & Zheng, H. Synthesis of metastable h-MoO<sub>3</sub> by simple chemical precipitation. *Mater. Chem. Phys.* **102**, 245–248, <https://doi.org/10.1016/j.matchemphys.2006.12.011> (2007).
- Sen, S. K. et al. Structural and optical properties of sol-gel synthesized h-MoO<sub>3</sub> nanorods treated by gamma radiation. *Nano Express* **1**, 020026, <https://doi.org/10.1088/2632-959X/aba4f8> (2020).
- da Silva Júnior, M. G. et al. A brief review of MoO<sub>3</sub> and MoO<sub>3</sub>-based materials and recent technological applications in gas sensors, lithium-ion batteries, adsorption, and photocatalysis. *Materials* **16**, 7657, <https://doi.org/10.3390/ma16247657> (2023).
- Sharma, R. et al. Synthesis & material properties of  $\alpha$ -MoO<sub>3</sub> nanoparticles. *Mater. Today Proc.* **48**, 683–686, <https://doi.org/10.1016/j.matpr.2021.08.092> (2022).
- Han, Y., Rheem, Y., Lee, K.-H., Kim, H. & Myung, N. V. Synthesis and characterization of orthorhombic-MoO<sub>3</sub> nanofibers with controlled morphology and diameter. *J. Ind. Eng. Chem.* **62**, 231–238, <https://doi.org/10.1016/j.jiec.2017.12.063> (2018).
- Sreedhara, M. B., Matte, H. S. S. R., Govindaraj, A. & Rao, C. N. R. Synthesis, characterization, and properties of few-layer MoO<sub>3</sub>. *Chem. –Asian J.* **8**, 2430–2435, <https://doi.org/10.1002/asia.201300470> (2013).
- Anjaneyulu, R. B., Mohan, B. S., Naidu, G. P. & Muralikrishna, R. Visible light enhanced photocatalytic degradation of methylene blue by ternary nanocomposite, MoO<sub>3</sub>/Fe<sub>2</sub>O<sub>3</sub>/rGO. *J. Asian Ceram. Soc.* **6**, 183–195, <https://doi.org/10.1080/21870764.2018.1479011> (2018).
- Rahman, M.d.H., Chowdhury, E. H. & Hong, S. High temperature oxidation of monolayer MoS<sub>2</sub> and its effect on mechanical properties: a ReaxFF molecular dynamics study. *Surf. Interfaces* **26**, 101371, <https://doi.org/10.1016/j.surfint.2021.101371> (2021).
- Reidy, K. et al. Atomic-scale mechanisms of MoS<sub>2</sub> oxidation for kinetic control of MoS<sub>2</sub>/MoO<sub>3</sub> interfaces. *Nano Lett.* **23**, 5894–5901, <https://doi.org/10.1021/acsnanolett.3c00303> (2023).
- Garadkar, K. M. et al. MoS<sub>2</sub>: preparation and their characterization. *J. Alloy. Compd.* **487**, 786–789, <https://doi.org/10.1016/j.jallcom.2009.08.069> (2009).
- Bouzidi, A. et al. Effect of substrate temperature on the structural and optical properties of MoO<sub>3</sub> thin films prepared by spray pyrolysis technique. *Mater. Sci. Eng. B* **97**, 5–8, [https://doi.org/10.1016/S0921-5107\(02\)00385-9](https://doi.org/10.1016/S0921-5107(02)00385-9) (2003).
- Ali, S. & Farrukh, M. A. Effect of calcination temperature on the structural, thermodynamic, and optical properties of MoO<sub>3</sub> nanoparticles. *J. Chin. Chem. Soc.* **65**, 276–288, <https://doi.org/10.1002/jccs.201700163> (2018).
- Viršek, M., Jesih, A., Milošević, I., Damjanović, M. & Remškar, M. Raman scattering of the MoS<sub>2</sub> and WS<sub>2</sub> single nanotubes. *Surf. Sci.* **601**, 2868–2872, <https://doi.org/10.1016/j.susc.2006.12.050> (2007).
- Li, H. et al. From bulk to monolayer MoS<sub>2</sub>: evolution of Raman scattering. *Adv. Funct. Mater.* **22**, 1385–1390, <https://doi.org/10.1002/adfm.201102111> (2012).
- Chakraborty, B., Matte, H. S. S. R., Sood, A. K. & Rao, C. N. R. Layer-dependent resonant Raman scattering of a few layer MoS<sub>2</sub>. *J. Raman Spectrosc.* **44**, 92–96, <https://doi.org/10.1002/jrs.4147> (2013).
- Siciliano, T., Tepore, A., Filippo, E., Micocci, G. & Tepore, M. Characteristics of molybdenum trioxide nanobelts prepared by thermal evaporation technique. *Mater. Chem. Phys.* **114**, 687–691, <https://doi.org/10.1016/j.matchemphys.2008.10.018> (2009).
- Diaz-Droguett, D. E., El Far, R., Fuenzalida, V. M. & Cabrera, A. L. In situ-Raman studies on thermally induced structural changes of porous MoO<sub>3</sub> prepared in vapor phase under He and H<sub>2</sub>. *Mater. Chem. Phys.* **134**, 631–638, <https://doi.org/10.1016/j.matchemphys.2012.03.042> (2012).

45. Wang, L., Li, H. & Xue, Z. Synthesis of h-MoO<sub>3</sub> nanorods and h- $\alpha$ -MoO<sub>3</sub> composites and their photocatalytic performance. *Trans. Nonferrous Met. Soc. China* **33**, 2155–2167, [https://doi.org/10.1016/S1003-6326\(23\)66250-8](https://doi.org/10.1016/S1003-6326(23)66250-8) (2023).
46. Lee, S.-H. et al. Raman spectroscopic studies of electrochromic  $\alpha$ -MoO<sub>3</sub> thin films. *Solid State Ion.* **147**, 129–133, [https://doi.org/10.1016/S0167-2738\(01\)01035-9](https://doi.org/10.1016/S0167-2738(01)01035-9) (2002).
47. Yang, X., Tang, H., Zhang, R., Song, H. & Cao, K. Synthesis of high-quality crystalline  $\alpha$ -MoO<sub>3</sub> nanobelts. *Crys. Res. Technol.* **46**, 409–412, <https://doi.org/10.1002/crat.201100061> (2011).
48. Sun, H. L. et al. One-step synthesis of centimeter-size  $\alpha$ -MoO<sub>3</sub> with single crystallinity. *Appl. Surf. Sci.* **476**, 789–795, <https://doi.org/10.1016/j.apsusc.2019.01.169> (2019).
49. Zakharova, G. S. et al. MoO<sub>3</sub>– $\delta$  nanorods: synthesis, characterization and magnetic properties. *Solid State Sci.* **9**, 1028–1032, <https://doi.org/10.1016/j.solidstatesciences.2007.07.022> (2007).
50. Chen, Y. et al. Single-crystalline orthorhombic molybdenum oxide nanobelts: synthesis and photocatalytic properties. *CrystEngComm* **12**, 3740, <https://doi.org/10.1039/c000744g> (2010).
51. Wongkrua, P., Thongtem, T. & Thongtem, S. Synthesis of h- and  $\alpha$ -MoO<sub>3</sub> by refluxing and calcination combination: phase and morphology transformation, photocatalysis, and photosensitization. *J. Nanomater.* **2013**, 1–8, <https://doi.org/10.1155/2013/702679> (2013).
52. Xia, T., Li, Q., Liu, X., Meng, J. & Cao, X. Morphology-controllable synthesis and characterization of single-crystal molybdenum trioxide. *J. Phys. Chem. B* **110**, 2006–2012, <https://doi.org/10.1021/jp055945n> (2006).
53. Guzman, G., Yebka, B., Livage, J. & Julien, C. Lithium intercalation studies in hydrated molybdenum oxides. *Solid State Ion.* **86–88**, 407–413, [https://doi.org/10.1016/0167-2738\(96\)00338-4](https://doi.org/10.1016/0167-2738(96)00338-4) (1996).
54. Sen, S. K. et al. Characterization and antibacterial activity study of hydrothermally synthesized h-MoO<sub>3</sub> nanorods and  $\alpha$ -MoO<sub>3</sub> nanoplates. *BioNanoScience* **9**, 873–882, <https://doi.org/10.1007/s12668-019-00671-7> (2019).
55. Hou, X. et al. Single-crystal MoO<sub>3</sub> micrometer and millimeter belts prepared from discarded molybdenum disilicide heating elements. *Sci. Rep.* **8**, 16771, <https://doi.org/10.1038/s41598-018-34849-y> (2018).
56. Aleksandrov, P. V. et al. Molybdenum recovery from molybdenite concentrates by low-temperature roasting with sodium chloride. *Int. J. Miner. Process.* **161**, 13–20, <https://doi.org/10.1016/j.minpro.2017.02.007> (2017).
57. Molybdenum Processing. <https://www.imoa.info/molybdenum/molybdenum-processing.php>.
58. Yi, G. et al. Recent progress on research of molybdenite flotation: a review. *Adv. Colloid Interface Sci.* **295**, 102466, <https://doi.org/10.1016/j.cis.2021.102466> (2021).
59. Huang, W., Tang, H., Cao, Y., Liu, R. & Sun, W. Separation of molybdenite from chalcopyrite with thiolactic acid depressant: flotation behavior and mechanism. *Trans. Nonferrous Met. Soc. China* **33**, 3157–3167, [https://doi.org/10.1016/S1003-6326\(23\)66324-1](https://doi.org/10.1016/S1003-6326(23)66324-1) (2023).
60. Yuan, D., Cadien, K., Liu, Q. & Zeng, H. Separation of talc and molybdenite: challenges and opportunities. *Miner. Eng.* **143**, 105923, <https://doi.org/10.1016/j.mineng.2019.105923> (2019).
61. Wang, L., Zhang, G., Dang, J. & Chou, K. Oxidation roasting of molybdenite concentrate. *Trans. Nonferrous Met. Soc. China* **25**, 4167–4174, [https://doi.org/10.1016/S1003-6326\(15\)64067-5](https://doi.org/10.1016/S1003-6326(15)64067-5) (2015).
62. Shalchian, H., Birloaga, I., Moghaddam, M. B., Nasiri, H. & Vegliò, F. “A hydro-metallurgical process flowsheet for recovering MoO<sub>3</sub> from Molybdenite. *Hydrometallurgy* **228**, 106355, <https://doi.org/10.1016/j.hydromet.2024.106355> (2024).
63. Fatheema, J. et al. A comprehensive investigation of MoO<sub>3</sub> based resistive random access memory. *RSC Adv.* **10**, 19337–19345, <https://doi.org/10.1039/D0RA03415K> (2020).
64. Sawa, A. Resistive switching in transition metal oxides. *Mater. Today* **11**, 28–36, [https://doi.org/10.1016/S1369-7021\(08\)70119-6](https://doi.org/10.1016/S1369-7021(08)70119-6) (2008).
65. Bharathi, M. et al. Effect of Ag doping on bipolar switching operation in molybdenum trioxide (MoO<sub>3</sub>) nanostructures for non-volatile memory. *J. Alloy. Compd.* **862**, 158035, <https://doi.org/10.1016/j.jallcom.2020.158035> (2021).
66. Xu, Y. et al. High-performance MoOx/n-Si heterojunction NIR photodetector with aluminum oxide as a tunneling passivation interlayer. *Nanotechnology* **32**, 275502, <https://doi.org/10.1088/1361-6528/abf37c> (2021).
67. Noby, S. Z. et al. Oxygen vacancies in oxidized and reduced vertically aligned  $\alpha$ -MoO<sub>3</sub> nanoblades. *Mater. Adv.* **3**, 3571–3581, <https://doi.org/10.1039/D1MA00678A> (2022).
68. Paparoni, F. et al. Unraveling oxygen vacancy formation, dynamics and site distribution in MoO<sub>3</sub>-x thin films. *Mater. Chem. Phys.* **333**, 130317, <https://doi.org/10.1016/j.matchemphys.2024.130317> (2025).
69. Lü, Z. et al. Ohmic contact and space-charge-limited current in molybdenum oxide modified devices. *Phys. E Low-Dimens. Syst. Nanostruct.* **41**, 1806–1809, <https://doi.org/10.1016/j.physe.2009.07.003> (2009).
70. Wang, Z., Huang, H. & Guo, X. Memristive devices with multiple resistance states based on the migration of protons in  $\alpha$ -MoO<sub>3</sub>/SrCoO<sub>2.5</sub> stacks. *Adv. Electron. Mater.* **7**, 2001243, <https://doi.org/10.1002/aeml.202001243> (2021).
71. Liu, D. & Robertson, J. Oxygen vacancy levels and interfaces of Al<sub>2</sub>O<sub>3</sub>. *Microelectron. Eng.* **86**, 1668–1671, <https://doi.org/10.1016/j.mee.2009.03.012> (2009).
72. Qin, J. et al. Improved resistive switching performance and mechanism analysis of MoO<sub>3</sub> nanorods based memristors. *Mater. Today Commun.* **36**, 106770, <https://doi.org/10.1016/j.mtcomm.2023.106770> (2023).
73. Shen, S., Liu, Y., Gordon, R. G. & Brillson, L. J. Impact of ultrathin Al<sub>2</sub>O<sub>3</sub> diffusion barriers on defects in high-k LaLuO<sub>3</sub> on Si. *Appl. Phys. Lett.* **98**, 172902, <https://doi.org/10.1063/1.3583462> (2011).
74. Rahman, F. et al. Reversible resistive switching behaviour in CVD grown, large area MoOx. *Nanoscale* **10**, 19711–19719, <https://doi.org/10.1039/C8NR04407D> (2018).
75. Rasool, A., Amiruddin, R., Mohamed, I. R. & Kumar, M. C. S. Fabrication and characterization of resistive random access memory (ReRAM) devices using molybdenum trioxide (MoO<sub>3</sub>) as switching layer. *Superlattices Microstruct.* **147**, 106682, <https://doi.org/10.1016/j.spmi.2020.106682> (2020).
76. Goul, R. et al. Atomic-scale tuning of ultrathin memristors. *Commun. Phys.* **5**, 260, <https://doi.org/10.1038/s42005-022-01037-4> (2022).
77. S. A. S. & R. V. Review of memristor based neuromorphic computation: opportunities, challenges and applications. *Eng. Res. Express* **6**, 032203 2024, <https://doi.org/10.1088/2631-8695/ad6662> (2024).
78. Kim, S. J., Kim, S. & Jang, H. W. Competing memristors for brain-inspired computing. *iScience* **24**, 101889, <https://doi.org/10.1016/j.isci.2020.101889> (2021).